Additive Manufacturing 35 (2020) 101362

Contents lists available at ScienceDirect

Additive Manufacturing

journal homepage: www.elsevier.com/locate/addma

Revealing transient powder-gas interaction in laser powder bed fusion process through multi-physics modeling and high-speed synchrotron x-ray imaging

Xuxiao Li[a], Cang Zhao[b,1], Tao Sun[b,2], Wenda Tan[a,*]

[a] Department of Mechanical Engineering, University of Utah, Salt Lake City, Utah, 84112, USA
[b] X-ray Science Division, Argonne National Laboratory, Lemont, Illinois, 60439, USA

ARTICLE INFO

Keywords:
Laser powder bed fusion
Powder motion
Powder-gas interaction
Multi-physics modeling
High-speed synchrotron x-ray imaging

ABSTRACT

Laser powder bed fusion (LPBF) is an emerging metal additive manufacturing process. The gas-driven powder motions in laser powder bed fusion have significant influence on the build quality. However, the transient powder-gas interaction has not been well understood due to the challenges in quantitative experiment measurements. In this work, the powder-gas interaction for a single pulse laser illuminating on the powder bed is studied. We establish a multi-physics model to simulate the complex liquid/gas flow as well as the gas-driven powder motions, which is substantiated by high-speed synchrotron x-ray imaging. We identify and quantify four characteristic modes of powder-gas interaction in LPBF. The motion of a powder is controlled by one or multiple interaction modes collectively. As revealed by simulations and confirmed by experiments, powders can merge into the molten pool from its rim, be ejected at different divergence angles (powder spattering), or dive into the molten pool to cause significant molten pool fluctuation. Our results provide insights toward the driving forces controlling the dynamic powder behavior, which pave the way for reducing structure defects during the build process.

1. Introduction

In a laser powder bed fusion (LPBF) process, a high-power laser scans across a thin layer of powders with tens of microns in size, locally melts the powders, and fuses them to the bottom layer. This process is then repeated in a layer-by-layer fashion until a three-dimensional part is consolidated. The additive nature makes LPBF capable of building parts with extremely complex geometries, which largely unleashes the design freedom. However, the laser-metal interaction gives rise to multiple transient thermo-fluid phenomena, and their complicated interplay often leads to structural defects in LPBF builds. One important phenomenon is the powder motions accompanying the laser melting [1–5]. It is found that powders in the bed have the tendency of being entrained towards the laser-illuminated region, and once entering the laser interaction zone, the entrained powders can be either incorporated into the molten pool or ejected abruptly towards different directions. These powder motions have significant impact on the build quality. For instance, the displacement of powders causes inhomogeneous mass distribution of the powder bed, which reduces the build accuracy [5]. The ejected powders eventually fall back onto the powder bed, which can increase the surface roughness [6] or even lead to lack-of-fusion defects [2,7]. Given the intrinsic complexity in powder motion [3] and the large number of events involved in LPBF, significant uncertainties exist in predicting and controlling the powder motions.

There have been substantial efforts made to understand the driving forces of powder motions in the hope that these motions can be controlled to improve the build quality and consistency. Among them, the direct observation of powder motions, via high-speed optical [3–5] and x-ray imaging [1,2], suggested that the powder entrainment is caused by the gas pressure difference between the laser zone and the ambient environment. The high-power laser evaporates the sample, which creates a high-velocity metal vapor jet expanding into the ambient protection gas (typically Argon). The recoil pressure on the melt surface then creates a depression. The vapor jet resembles a free jet in classical boundary layer theory to induce an (ambient) Argon flow that carries the surrounding powders to move towards the jet center. If the

* Corresponding author.
E-mail address: wenda.tan@mech.utah.edu (W. Tan).
[1] Currently at the Department of Mechanical Engineering, Tsinghua University, Beijing, China.
[2] Currently at the Department of Materials Science and Engineering, University of Virginia, Charlottesville, VA, USA.

https://doi.org/10.1016/j.addma.2020.101362
Received 22 January 2020; Received in revised form 6 April 2020; Accepted 26 May 2020
Available online 15 June 2020

entrained powders touch the molten pool, they are melted and incorporated into the build; otherwise, they tend to be ejected by the metal vapor.

The above understanding regarding the gas-driven powder motions is formulated from basic principles of thermo-fluid physics which rationalizes some observations. The detailed structure of the transient gas (vapor jet and Argon) flow, as well as the powder-gas interactions are commonly examined using analytical calculations with significant simplifications. However, quantitative information regarding the gas flow field and powder-gas interactions (e.g., gas-flow-induced force distribution on powder surface) is still needed to understand and control the complex powder motions in LPBF. Such information is generally difficult to obtain in experiments. Visible-light and x-ray imaging may capture the powder trajectories, yet the gaseous phase does not yield discernable contrast. Schlieren imaging is particularly sensitive to vapor plume structures [3,34], but the subtle motions of powers can be difficult to trace. Although combining multiple imaging techniques can potentially observe the powder-gas interaction, quantifying the motions of a large number of powders in LPBF remains challenging.

Multi-physics simulations can therefore serve as an effective approach for studying gas-powder interaction in LPBF. By now, the major efforts of mesoscale multi-physics simulation have been focused on the molten pool dynamics [8–10]. A few other works simulated the gas flow in its steady state without considering the molten pool dynamics [3,11]. In a recent work [12], both the transient dynamics of molten pool and gas flow are simulated, but powders are not included in their model. To the best of our knowledge, no simulation work has been reported regarding the powder-gas interaction in LPBF. The major challenge of simulating the powder-gas interaction is the highly coupled physics between the condensed phase (liquid and solid metal) and the gaseous phase (vapor metal and protection gas) in LPBF. The thermo-fluid dynamics of the high-speed compressible gaseous phase, the low-speed incompressible metal phase, and the rigid-body motion of the individual powders must be simultaneously simulated in order to capture the complex physics.

In this work, we significantly expand our prior works [13–15] to enable the multi-physics modeling for LPBF. Specifically, we utilized a unified algorithmic framework [16] to treat both compressible and incompressible flows. Within this framework, the level-set method [17], the Lagrangian particle tracking [18], and the ghost fluid method [13,19] are synergistically integrated to model the complex physics in LPBF, i.e., molten pool dynamics, gas flow, powder motion, etc. While the model is currently in a two-dimensional (2D) form, the result indicates that it can successfully capture the key phenomena in LPBF, including the formation of depression zone, melt flow, vapor generation, and plume development. Furthermore, the transient powder-gas interaction can be quantitatively investigated by calculating the flow field surrounding the powders and the force distribution on the powder surface. From these simulations, we identify four characteristic modes of the powder-gas interaction, with each mode contributing to distinct powder motions. High-speed synchrotron x-ray imaging is used to substantiate the findings from the simulations.

2. Model description and experimental setup

2.1. Multi-physics simulation

The methodology of the multi-physics simulations is demonstrated in Fig. 1. The 2D computation domain can be divided into the condensed (metal) phase and the gaseous phase. The condensed phase includes the bulk solid metal (referred to as the substrate), the molten pool, and the individual powders (either solid or molten). The gaseous phase is a mixture of the metal vapor and the protection gas (Argon). The entire calculation domain is discretized by a Eulerian, Cartesian mesh in which the conservation equations are solved by a Computational Fluid Dynamics (CFD) solver to obtain the pressure, velocity, and temperature fields. The evolution of the interface between the condensed and the gaseous phase (referred to as the C–G interface) is captured by the level-set function defined on the Eulerian mesh. The ghost fluid method is utilized to coordinate the CFD computations in the condensed and the gaseous phase. The rigid-body powder motions are explicitly tracked by a Lagrangian Particle Tracking (LPT) technique to obtain the forces, velocities, and positions of the powders. The coordination between the LPT and CFD computations are achieved by the "Lagrangian points" defined on the powder surface (Fig. 1). The simulation progresses in discrete time steps. For each time step, the pressure, velocity, temperature, level-set function, and the powder information are predicted by an appropriate arrangement of the CFD, level-set, and LPT computations. Then, the computations are repeated for the next time step.

2.1.1. Computational fluid dynamics

The governing equations to be solved are the conservation equations of mass, momentum, and energy, as written in Eq. 1–3.

$$\frac{\partial \rho}{\partial t} + \nabla\cdot(\rho\vec{V}) = 0. \tag{1}$$

$$\frac{\partial}{\partial t}(\rho\vec{V}) + \nabla\cdot(\rho\vec{V}\vec{V}) = -\nabla p + \nabla\cdot\tau + \rho\vec{g}. \tag{2}$$

$$\frac{\partial}{\partial t}(\rho e) + \nabla\cdot(\rho e\vec{V}) = \nabla\cdot(p\vec{V}) + \nabla\cdot(\tau\vec{V}) + \rho\vec{g}\cdot\vec{V} + \nabla\cdot(k\nabla T). \tag{3}$$

The governing equations (Eqn. 1–3) are written in a general format to cope with both compressible (gaseous phase) and incompressible (condensed phase) flows. In Eqn. 1–3, ρ is the density, $\vec{V}$ is the velocity, p is the pressure, τ is the viscous tensor, $\vec{g}$ is the gravitational acceleration, e is the total energy (internal energy and kinetic energy), k is the thermal conductivity, and T is the temperature. Among these variables, we choose (p, $\vec{V}$, T) to be the primitive variables, and express the other variables (ρ, τ, e, k) as functions of (p, $\vec{V}$, T). It is the primitive variables that will eventually be solved from Eqn. 1–3.

In the condensed phase region, consistent velocity between the solid and liquid (molten) metal is enforced by adding Darcy's damping force [20], S_D, to the right side of Eq. 2:

$$S_D = -\frac{\mu_l}{K}\frac{\rho}{\rho_l}(\vec{V} - \vec{V_s}) \tag{4}$$

In Eqn. 4, μ_l and ρ_l are the viscosity and density of the liquid metal. $\vec{V_s}$ is a pre-defined velocity for the solid; $\vec{V_s}$ is set to be equal to the powder velocity (tracked by LPT technique) if the cell centroid is within powders, and is equal to zero elsewhere. K is a damping coefficient and is a function of temperature T.

The finite volume method is implemented to numerically solve Eqn. 1–3 in an implicit, fully-coupled manner [16]. Specifically, the preconditioning technique [21] is utilized to enable a unified treatment for both the low-speed, incompressible flow in the condensed phase and the high-speed, compressible flow in the gaseous phase. By virtue of the preconditioning technique, the primitive variables on the entire Eulerian mesh is solved with a single CFD solver for each time step of the simulation.

2.1.2. Multiphase computation

Important physics, including laser absorption, surface tension, and metal evaporation, occur at the dynamically evolving C–G interface and drive the subsequent physical phenomena in LPBF. Therefore, the interface evolution and the interfacial physics must be carefully considered. The level-set function ϕ is used to capture the interface whose evolution is governed by the level-set equation [17]:

$$\frac{\partial \phi}{\partial t} + \vec{V}\cdot\nabla\phi = 0 \tag{5}$$

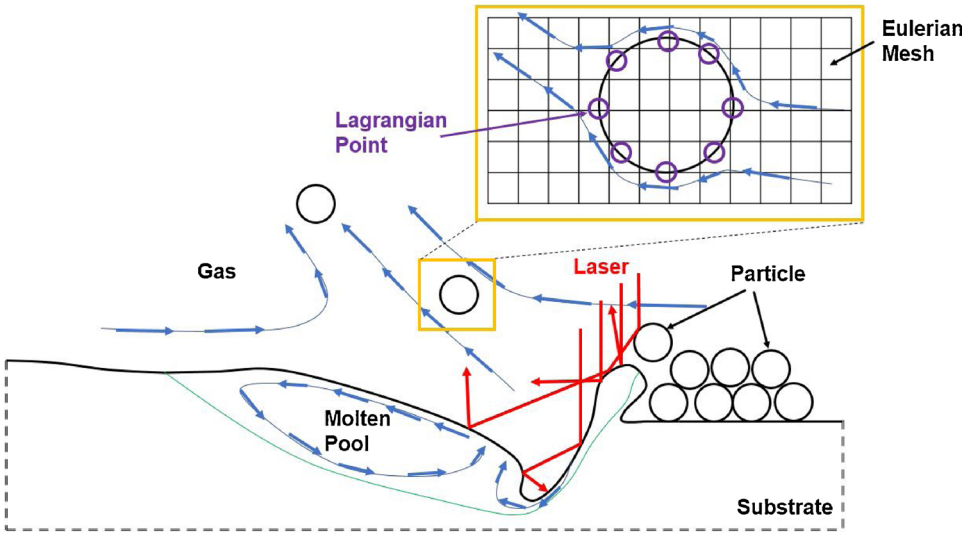

Fig. 1. Illustration of the simulation methodology.

The level-set equation is numerically solved by a standard finite difference method, with a second-order essentially non-oscillatory spatial discretization [17] and a second-order total variation diminishing Runge-Kutta temporal discretization [17].

Once the level-set function is solved, each cell can be identified to be either in the condensed phase region (C cell) or in the gaseous phase region (G cell) according to the sign of the level-set function (Fig. 2). The ghost fluid method [19] is then used to coordinate the CFD computations between these two sets of cells. With the ghost fluid method, the original mesh is split into two copies, one for the condensed phase (C-mesh) and the other for the gaseous phase (G-mesh), as shown in Fig. 2. For the C-mesh, the cells in the condensed phase ($\phi < 0$, marked black) are referred to as the real C cells in which the primitive variables are solved by the CFD computations. The cells right outside the condensed phase (marked red) are referred to as the ghost C cells whose primitive variables are specifically assigned as the boundary conditions. The rest of the C cells in C-mesh (marked gray) are deactivated and do not participate in any computation. The same approach applies for the G-mesh.

The assignment of the primitive variables for ghost C cells and ghost G cells is based on a series of computations in order to reflect the laser absorption, surface tension, and metal vaporization at the C–G interface. The ray-tracing method [22] is used to compute the absorbed heat flux on the C–G interface. The surface tension is computed from the interface curvature which is obtained from the level-set function. The temperature-dependency of the surface tension coefficient (Marangoni effect) is considered by modifying the viscous force at the C–G interface [23]. Finally, the evaporation kinetics of metal is considered with Knight's model [24]. More computation details can be found in [13,14].

2.1.3. Lagrangian particle tracking

The initial powder bed configuration is generated by a random packing algorithm [25,26]. Thereafter, the evolution of the velocities of each powder is tracked by solving Newton's equations of motion [18] (Eqn. 5 and 6):

$$m_p \frac{d\vec{V}_{pc}}{dt} = \oint_{\partial S} \vec{F_f}\, dS + m_p \vec{g} + \vec{F_{\text{col}}} \tag{5}$$

$$I_p \frac{d\vec{\omega}_p}{dt} = \oint_{\partial S} \vec{r} \times \vec{F}_f\, dS \tag{6}$$

Eqn. 5 governs the translational motion of the powder where m_p is the

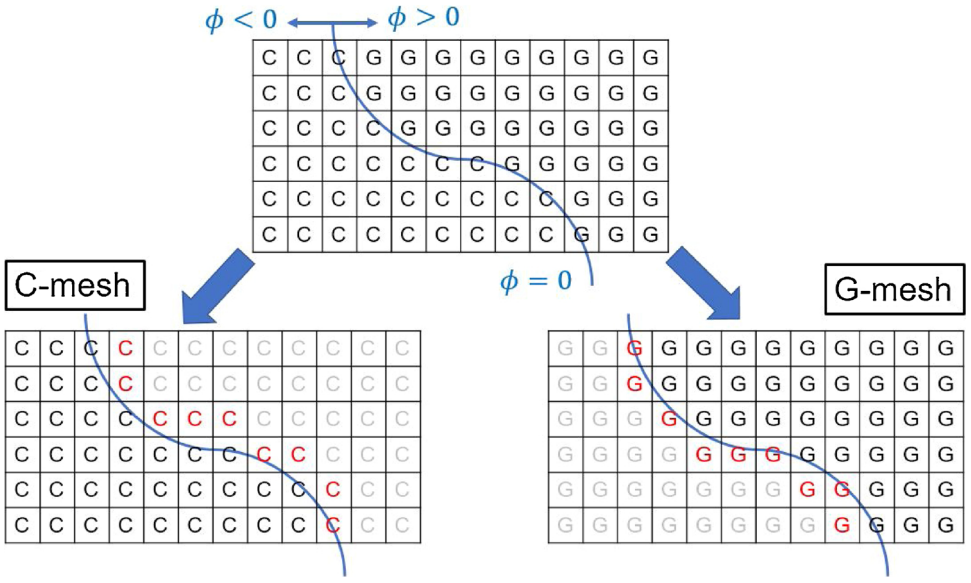

Fig. 2. Level-set and ghost fluid method.

Table 1
Material properties of Ti-6Al-4 V used for simulation.

Material property	Value	Unit
Solid heat capacity	670	J kg^{-1} K^{-1}
Liquid heat capacity	831	J kg^{-1} K^{-1}
Solid density	4420	kg m^{-3}
Liquid density	3920	kg m^{-3}
Latent heat of fusion	2.86×10^5	J kg^{-1}
Latent heat of vaporization	9.83×10^6	J kg^{-1}
Solidus temperature	1877	K
Liquidus temperature	1923	K
Viscosity	0.03	Pa s
Surface tension at liquidus temperature	1.525	N m^{-1}
Temperature coefficient of surface tension	-2.8×10^{-4}	N m^{-1} K^{-1}
Refractive index	3.47	
Extinction coefficient	4.01	
Boiling temperature at 1 atm	3533	K
Thermal expansion coefficient	1.96×10^{-5}	K^{-1}

particle mass and $\vec{V}_{pc}$ is the velocity of the powder center. On the right side, the first term is the integration of the gas-flow-induced force ($\vec{F_f}$) on the powder surface (∂S); the second term is the gravitational force, and the third term is the force due to powder-powder or powder-substrate collision. Eqn. 6 governs the rotational motion of the powder where I_p is the momentum of inertia and $\vec{\omega}_p$ is the angular velocity of the powder. The right side is the gas-flow-induced torque ($\vec{r}$ is the position vector) on the powder surface.

In this work, the collision is considered with a simplified model in which the collision force $\vec{F}_{\text{col}}$ is a short-range repulsive force [27] and the torque resulted from collisions are neglected. The gas-flow-induced force ($\vec{F_f}$) is evaluated using the "Lagrangian points" which are defined on the powder surface (Fig. 2) and are fixed relative to the powder frame. The pressure and the gradient of velocity are obtained from the CFD computations on the Eulerian mesh, and they are used to interpolate the $\vec{F_f}$ (including pressure and viscous stress) on the Lagrangian points. Finally, the integrations on the right side of Eqn. 6 and 7 are numerically evaluated by the summation over all Lagrangian points of the powder.

Once the force and torque are evaluated for the right side of Eqn. 6 and 7, the powder velocities ($\vec{V}_{pc}$, $\vec{\omega}_p$) are advanced one time step further with a third-order Adam-Bashforth scheme [28]. The position of the powder center (x_{pc}, y_{pc}) and the angular position of the powder (θ_p) are then advanced using the previous velocities and with a third-order Adam-Bashforth scheme.

2.1.4. Arrangement of computations

We illustrate the arrangement of the computations by assuming that the simulation has progressed to the n^{th} time step, t^n. At this time step, the primitive variables (p, $\vec{V}$, T), level-set function (ϕ), and powder information ($\vec{V}_{pc}$, $\vec{\omega}_p$, x_{pc}, y_{pc}, θ_p) have already be computed, denoted as (p, $\vec{V}$, T, ϕ, $\vec{V}_{pc}$, $\vec{\omega}_p$, x_{pc}, y_{pc}, θ_p)^n. Based on (p, $\vec{V}$, T, ϕ, $\vec{V}_{pc}$, $\vec{\omega}_p$, x_{pc}, y_{pc}, θ_p)^n, the information at the next time step t^{n+1} are computed, which is outlined as follows.

- Step 1: Interpolate the gas-flow-induced force on Lagrangian points from (p, $\vec{V}$)^n on the Eulerian mesh.
- Step 2: Update the powder information to obtain ($\vec{V}_{pc}$, $\vec{\omega}_p$, x_{pc}, y_{pc}, θ_p)$^{n+1}$ by solving Eqn. 6 and 7 with LPT.
- Step 3: Update the level-set function by solving Eqn. 4 with $\vec{V}^n$ to obtain ϕ^{n+1}.
- Step 4: With the updated level-set function and powder positions, create the C-mesh and G-mesh, and identify real and ghost cells.
- Step 5: Assign the primitive variables in the ghost cells as the boundary conditions for the subsequent CFD computation.
- Step 6: With the boundary condition defined in ghost cells, solve Eqn. 1–3 in both the C-mesh and the G-mesh with CFD to obtain (p, $\vec{V}$, T)$^{n+1}$.
- Step 7: The entire package of (p, $\vec{V}$, T, ϕ, $\vec{V}_{pc}$, $\vec{\omega}_p$, x_{pc}, y_{pc}, θ_p)$^{n+1}$ has been obtained. Go back to Step 1 and repeat.

2.2. High-speed synchrotron x-ray imaging

High-speed synchrotron x-ray imaging experiment on LPBF was performed at the 32-ID-B beamline of the Advanced Photon Source at Argonne National Laboratory. Detailed information on the imaging technique, beamline components, and the LPBF simulator was reported previously [1,29]. Briefly, an intense polychromatic x-ray beam generated from a short-period undulator was used in the imaging experiment. The first harmonic energy of the x-rays is ~24 keV. The detector system consists of a LuAG:Ce scintillator, a set of optics, and a high-speed visible-light camera (Photron SA-Z). The laser system integrates a 500 W ytterbium fiber laser (IPG YLR-500-AC, maximum output power 520 W), a laser head (IPG FLC 30), a stainless steel vacuum chamber, and a couple of sets of stepping motors. The laser beam has a $1/e^2$ diameter of ~220 μm on the sample surface. The miniature Ti-6Al-4 V powder bed samples were made manually. Two pieces of glassy carbon plates were used to contain a thin metal plate and a layer of metal powders on top. The thickness of the metal plate along the x-ray incidence direction is about 420 ~ 480 μm. In the experiment, the x-ray shutters, the imaging detector, and the laser system were triggered sequentially in order to capture the dynamic LPBF process. Argon (1 atm) was used as the protection gas. All results shown in this contribution were spot-weld type laser melting, i.e. stationary laser beam.

3. Results

3.1. Exemplary results from multi-physics simulations and high-speed X-ray imaging experiments

Here we study the physical scenario where a stationary laser is illuminated on a Ti-6Al-4 V powder bed with a thickness of 150 μm. The material properties used for the simulations are listed in Table 1 and 2. We employ comparable laser power density (~1.12 MW/cm^2), laser beam size (~ 150 μm), and powder size (~ 30 μm) in multi-physics simulations. We set the laser shining on 20 different locations of a large virtual powder bed to obtain 20 independent simulation results, such that the variation in the initial configuration of the powder bed can be captured. Exemplary time sequences of simulation and experiment results are shown in Fig. 3a and Fig. 3b, respectively. A side-by-side comparison of the corresponding movies is given in Supplementary Movie 1.

It can be observed in Fig. 3 that, after the sample is exposed to the laser, the metal powders melt and merge into a molten pool. The laser heating further induces metal vaporization on the molten pool surface, which leads to the formation of a vapor jet escaping the sample and a depression zone in the molten pool. The depression zone, driven by the balance of recoil pressure and surface tension, further evolves into a keyhole shape. The metal vapor jet induced Argon gas flow, which causes the entrainment and ejection of metal powders. The simulation, although in 2D, can in general predict the experimentally observed phenomena. In addition, the simulation can provide quantitative information on the temperatures and velocity fields of different phases to facilitate further analysis and understanding. These parameters are extremely difficult to measure directly in experiments. Here we also point out two major discrepancies between simulations and experiments: (1) Due to lack of the third dimension, simulations involve fewer powders than experiments. (2) Depth of the depression zone develops faster in simulations than in experiments due to the lack of resistance by surface tension from the third dimension.

Table 2
Material properties of Argon used for simulation.

Material property	Value	Unit
Specific heat under constant pressure, c_p	520	J kg^{-1} K^{-1}
Specific gas constant, R_s	208	J kg^{-1} K^{-1}
Prandtl number, P_r	0.68	
Reference temperature in Sutherland's law, T_r	280	K
Reference viscosity in Sutherland's law, μ_r	2.16 × 10^{-5}	Pa s
Sutherland temperature, S	160	K
Density, ρ	Temperature (T) and pressure (p) dependent, ideal gas law: $\rho = \frac{p}{R_S T}$	kg m^{-3}
Viscosity, μ	Temperature (T) dependent, Sutherland's law: $\mu = \mu_r \left(\frac{T}{T_r}\right)^{1.5} \frac{T_r + S}{T + S}$	Pa s

3.2. Characteristic modes of powder-gas interaction

From the typical time sequence of simulation results shown in Fig. 3a, we extract four key time frames: 35 us, 110 us, 145 us, and 165 us to demonstrate four characteristic modes of powder-gas interaction, which we define as "recoil mode", "entrainment mode", "elevation mode", and "expulsion mode", respectively. For each mode, we analyze different physical quantities as shown by the rows of Fig. 4. The first row shows the laser absorption distribution on the metal surface. The second row shows the temperature and velocity field. The third shows the field of gauge pressure (the difference between the absolute and the atmospheric pressure). The last row shows the forces acting on the powder surface. For the force analysis, the red and blue dashed lines along with the small arrows indicate the pressure and viscous stress distribution on the powder surface. The total force resulted from pressure ($\overrightarrow{F_p}$) and viscous stress ($\overrightarrow{F_v}$) are represented by the big red and blue arrows pointing from powder center to powder rim, and their sum, $\overrightarrow{F_{tot}} = \overrightarrow{F_p} + \overrightarrow{F}_v$, is indicated by the big black arrow. We note that the big arrows only show the directions of the forces, and their magnitudes are indicated by the numbers in Fig. 4m – 4p. The four modes of powder-gas interaction are distinctly defined by the different mechanisms that dominate the total force of the powder, as detailed below.

The "recoil mode" is defined when metal vaporization dominates the total force of the powder, which is pointing downwards (Fig. 4m). It typically occurs for the powder initially exposed to the laser beam (Fig. 4a). The local metal vaporization generates a large recoil pressure ($\gtrsim$ 20,000 Pa) on the top surface of the powder. The recoil pressure is a boundary condition that can only be marked out in Fig. 4m but cannot be visualized in the spatial distribution of gauge pressure in Fig. 4i. In this case the recoil pressure is significantly larger than the gauge pressure around the particles. It dominates the pressure-induced force that is pointing downward with a large magnitude ($|\overrightarrow{F_p}| = 0.193$ N, the big red arrow in Fig. 4m). On the other hand, the gas flow surrounding the flow is rather weak except for the evaporation flux on the top surface (Fig. 4e), which creates a negligible viscous force ($|\overrightarrow{F_v}| = 0.021$ N, the big blue arrow in Fig. 4m). Therefore, the total force for this powder in the recoil mode ($|\overrightarrow{F_{tot}}| = 0.190$ N, the big black arrow in Fig. 4m) will abruptly push the powder downward. The recoil mode interaction typically lasts only tens of microseconds, as the powders in this mode are usually in the liquid state and can soon merge into the molten pool (t = 35 ~ 60 μs in Fig. 3a).

The "entrainment mode" is defined when the entrained Argon gas flow dominates the total force of the powder, which is pointing towards the vapor jet (Fig. 4n). It applies to those powders that move towards the quasi-steady vapor jet center from the vicinity (t = 85 ~ 110 μs in Fig. 3a). For the typical powder studied at t = 110 μs (Fig. 4b), the vapor jet creates a lower pressure (~ −2000 Pa) on the right side than the one on the left side (~ 500 Pa) of the powder (Fig. 4j). This pressure gradient drives the pressure-induced force pointing toward the vapor jet ($|\overrightarrow{F_p}| = 0.039$ N, the big red arrow in Fig. 4n). In the meantime, this pressure gradient also induces an entrained Argon flow toward the vapor jet at ~ 10 m/s (Fig. 4f), which causes the viscous force pointing along the stream direction towards the vapor jet ($|\overrightarrow{F_v}| = 0.012$ N, the big blue arrow in Fig. 4n). As a result, the total force for this powder in the entrainment mode ($|\overrightarrow{F_{tot}}| = 0.048$ N, the big black arrow in Fig. 4f) will drive the powder to move toward the vapor jet at a velocity of ~ 0.7 m/s.

The "elevation mode" is defined when the entrained Argon gas flow and the vapor jet flow collaboratively determine the total force of the powder, which is pointing vertically upwards (Fig. 4o). It occurs when the entrained powder touches the edge of the vapor jet. For the powder studied at t = 145 μs (Fig. 4c), the edge of the vapor jet flows across the powder surface (Fig. 4g) at a vertical velocity of ~ 200 m/s and drives the powder to move upward through viscous stress ($|\overrightarrow{F_v}| = 0.122$ N, the big blue arrow in Fig. 4o). The distribution of gauge pressure around the powder is somewhat complex (Fig. 4k). The lower-right corner of the powder partially blocks the expansion of the vapor jet, and the loss of vapor momentum creates a high-pressure region (~ 3000 Pa). The upper-right corner of powder is a low-pressure region (~ -3000 Pa) towards which the Argon gas can continue to push the powder. This complex pressure distribution generates an upward pressure-induced force ($|\overrightarrow{F_p}| = 0.060$ N, the big red arrow in Fig. 4o). The total force is ($|\overrightarrow{F_{tot}}| = 0.182$ N, the big black arrow in Fig. 4o) will drive the powder to elevate while keeping its horizontal velocity.

The "expulsion mode" is defined when the vapor jet flow dominates the total force of the powder, which deviates from the upward-pointing direction with a certain angle (Fig. 4p). It refers to the occasions when the powders manage to enter the vapor jet. The powder studied at t = 165 μs significantly blocks the expansion of the vapor jet (Fig. 4h). A high-pressure region is formed (~ 20,000 Pa) at the lower-right corner of the powder (Fig. 4l) due to the blockage, which drives the pressure-induced force to point toward the upper left direction ($|\overrightarrow{F_p}| = 0.393$ N, the big red arrow in Fig. 4p). The high-speed vapor flow (~ 350 m/s, Fig. 4h) also exerts a viscous force along its streaming direction ($|\overrightarrow{F_v}| = 0.317$ N, the big blue arrow in Fig. 4p). Driven by the total force ($|\overrightarrow{F_{tot}}| = 0.710$ N, the big black arrow in Fig. 4p), the powder starts to be expelled towards a certain angle (~ 20 degrees) from the laser beam, with the ejection velocity reaching ~ 10 m/s eventually (t = 190 μs in Fig. 3a).

Here we iterate that the four different modes of powder-gas interaction are distinctly defined by the different mechanisms that dominate the total force of the powder. The "recoil mode" occurs when local vaporization generates dominating recoil pressure to drive the total force downward. The "entrainment mode" occurs when the entrained Argon gas flow dominates to drive the total force pointing toward the vapor jet. The "elevation mode" occurs when the entrained Argon gas flow and the vapor jet flow have comparable influence on the powder motion, and hence the total force is pointing vertically upward. The

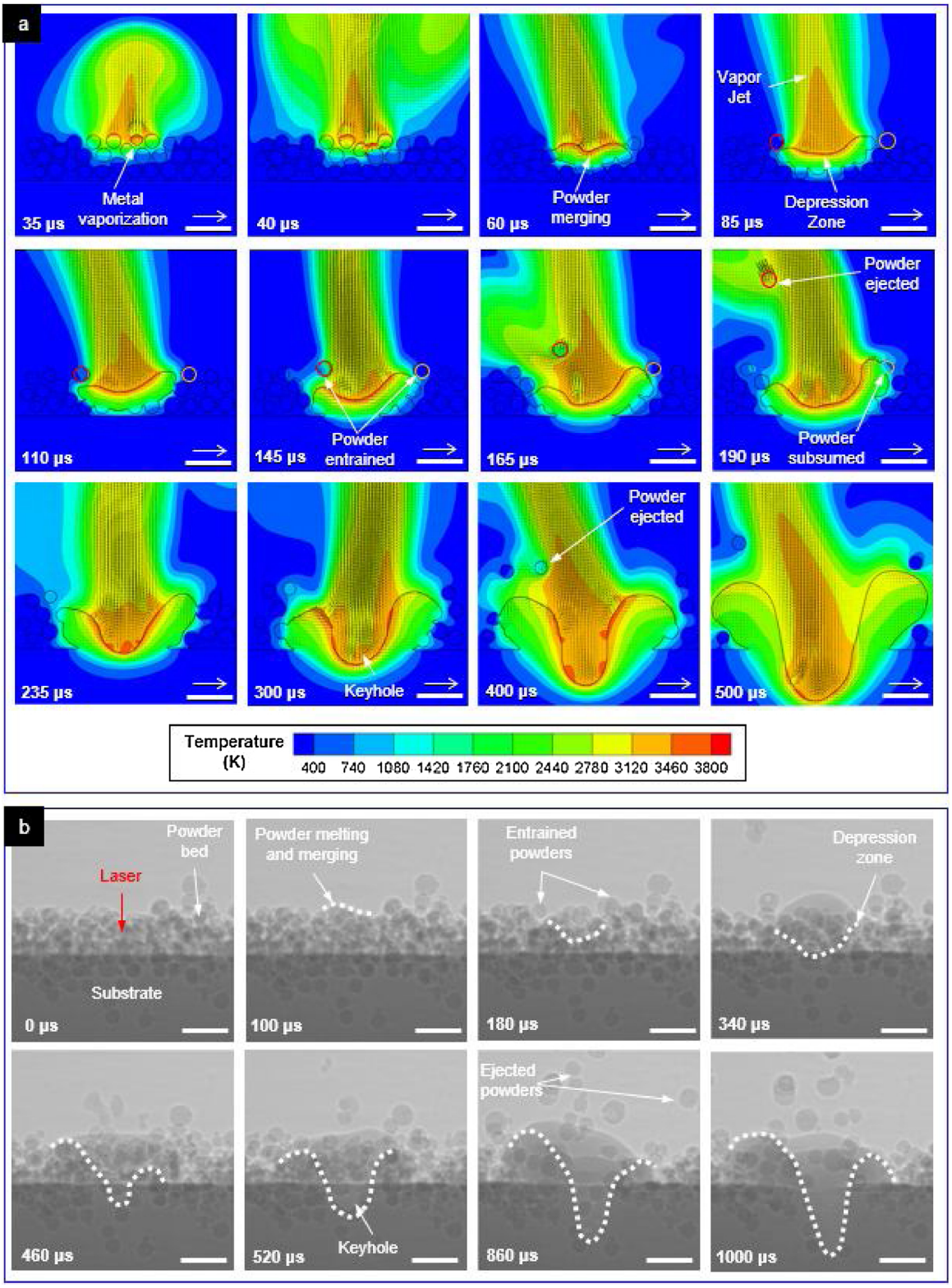

Fig. 3. Typical time sequences from multi-physics simulations, (a) and high-speed X-ray imaging experiments, (b). In each time frame, the elapsed time after the laser is turned on is indicated at the lower left corner. All scale bars are in 100 μm. In (a), the color contour shows the temperature field and the vectors show the velocity field. The arrow key is 20 m/s for the condensed phase and 2000 m/s for the gaseous phase. The simulation in 2D can in general predict the experimentally observed phenomena of powder melting and merging, the formation and evolution of the molten pool and depression zone, as well as the powder entrainment and ejection induced by the gas flow.

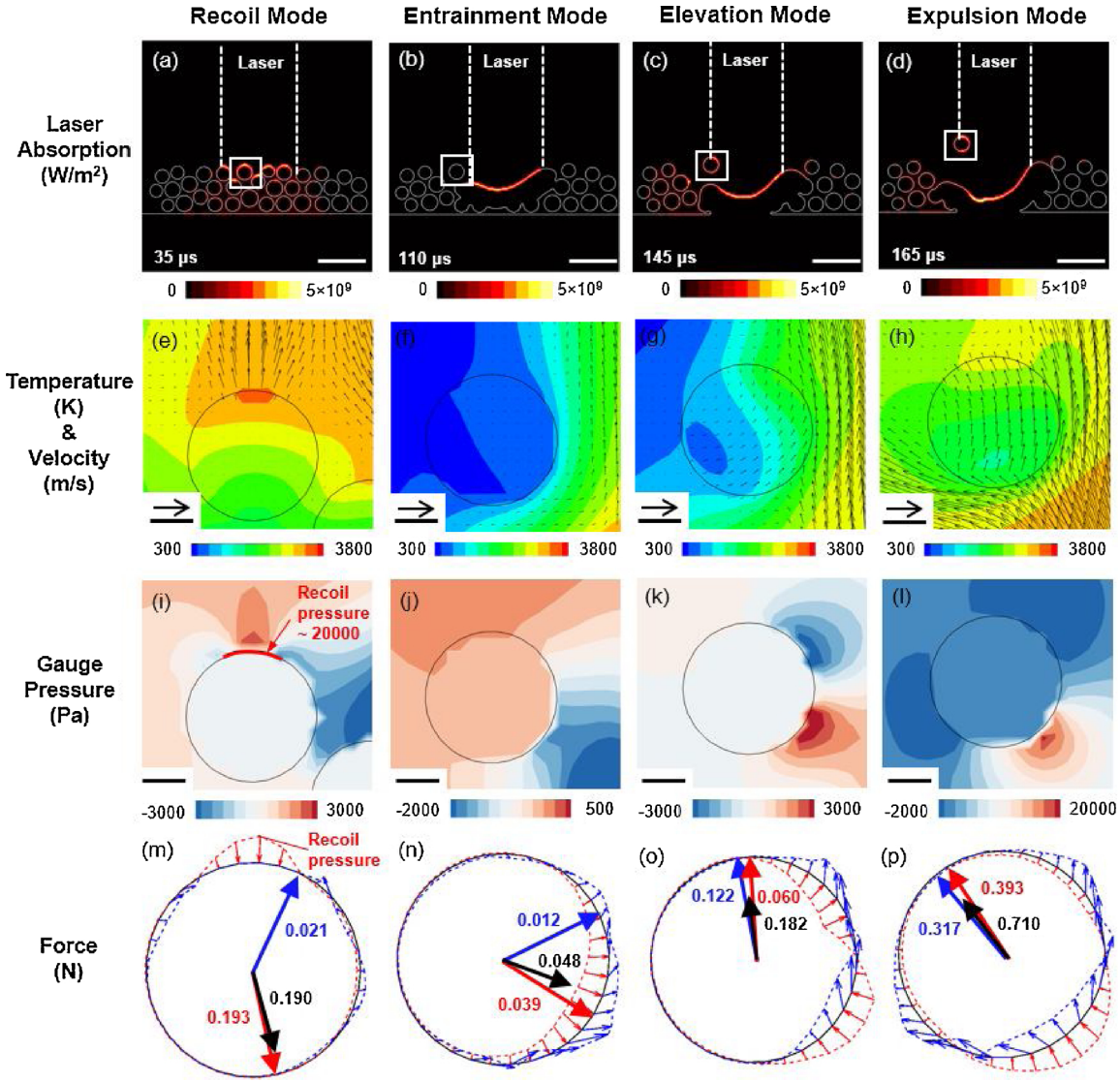

Fig. 4. Quantitative analysis of the powder-gas interaction. (a) – (d) laser absorption distribution on powder and molten pool surface. The time frames are extracted from the result in Fig. 3a and the scale bar is 100 μm. The white box indicates the powders under investigation and the white-dashed line shows the laser diameter. (e) – (h) the temperature and velocity field around the powder. The scale bar is 10 μm, and the key arrow is 20 m/s for the condensed phase and 500 m/s for the gaseous phase. (i) – (l) the gauge pressure distribution around the powder. The scale bar is 10 μm. The recoil pressure due to vaporization is not visualized in (i) but is shown in (m). (m) – (p) different forces acting on the powder surface. The red and blue dashed lines along with the small arrows indicate the pressure and viscous stress. The big red and blue arrows indicate the forces resulted from pressure and viscous stress. The big black arrow indicates the total force.

"expulsion mode" occurs when the powder enters the vapor jet, which hence dominates the powder motion and drives the total force upward with a divergence angle.

3.3. Powder motions governed by different mode(s)

During the lifespan of a powder (i.e., before fully melted or ejected away from powder bed), its motion can be governed by either a single dominating mode of powder-gas interaction or by a sequence of modes. For example, the powder studied in Fig. 4a is only subject to the recoil mode, and it promptly moves downward and merges into the molten pool (t = 35 ~ 60 μs in Fig. 3a). The orange-circled powder in Fig. 3a only experiences the entrainment mode, and it moves towards the vapor jet and then merges into the molten pool. The red-circled powder in Fig. 3a, however, is sequentially subject to the entrainment, elevation, and expulsion mode, leading to its entrainment-ejection motion. In the total 20 simulations, we have also identified other powder motions governed by one or more modes, which are presented in this section.

The elevation and expulsion modes can be found as the dominating mode that governs the powder behaviors. The examples of such cases are shown in Fig. 5a and b and the corresponding movies are given in Supplementary Movie 2 and 3. In Fig. 5a, the elevation mode dominates the powder-gas interaction for the powders initially located just at the edge of the vapor jet (the red- and orange-circled powders). As analyzed in Fig. 4g, 4k, and 4o, the net force from both the viscous stress and the pressure are pointing dominantly upwards for the elevation mode. As a result, the powders are ejected almost vertically as soon as the vapor jet is formed. In Fig. 5b, the expulsion mode dominates the powder-gas interaction when the red-circled are directly impacted by a tilted vapor jet. Due to the initial random powder configuration, the molten pool is always unsymmetrical as the mass cannot be uniformly distributed with respect to the laser center. In this particular example, more mass is accumulated on the left side of the molten pool, resulting in the vapor jet tilted towards the right. Therefore, the red-circled powder is directly impacted by the expanding vapor jet without being entrained into the laser-illuminated region. The powder is then ejected along the tilting

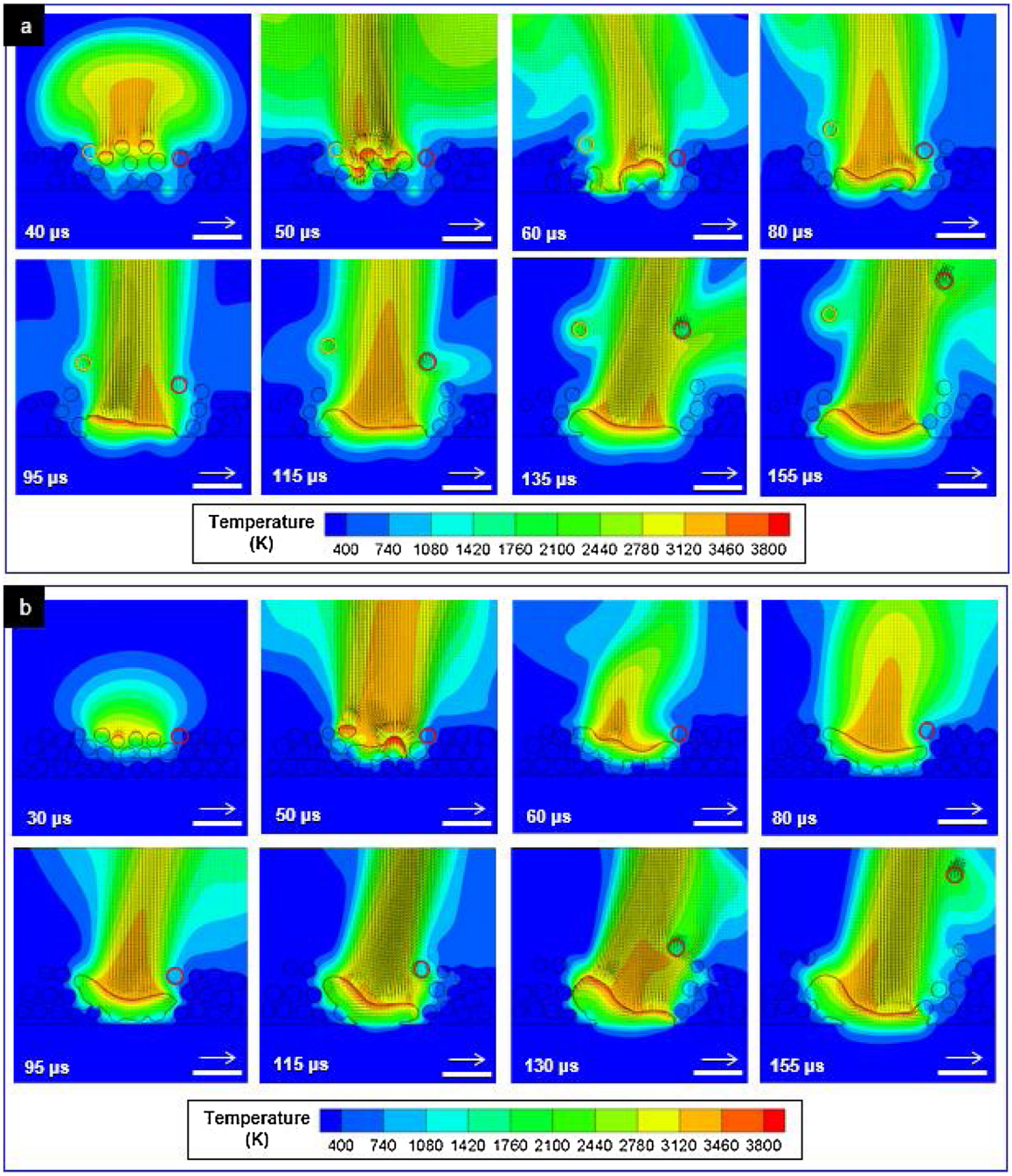

Fig. 5. Two time sequences of the simulation results to demonstrate that the elevation mode (a) and the expulsion mode (b) can dominate the powder-gas interaction. (a) The red- and orange-circled powders are initially located at the edge of the vapor jet when the latter is formed (t = 40 ~ 60 μs), and they are ejected almost vertically. (b) The red-circled powder is directly impacted by the tilted vapor jet (t = 130 μs) and is ejected along the tilting direction. All the scale bars are 100 μm, and all the arrow keys are 20 m/s for the condensed phase and 2000 m/s for the gaseous phase.

direction of the vapor jet.

It has also been found that the recoil mode can interrupt the elevation/expulsion mode to cause the "diving" motion of powder. One example of this case is shown in Fig. 6, with the corresponding movie given in Supplementary Movie 4. The red-circled powder is subject to the entrainment mode and reaches the edge of the vapor jet at t = 245 μs. The powder is then subject to the elevation mode at t = 265 μs and should have been subject to the expulsion mode at t = 285 μs to be ejected away. However, as the powder is heated by the laser beam, local vaporization occurs at the top surface of the powder (t = 285 μs), and soon becomes intense due to the lack of heat sink (t = 295 μs). As a result, the recoil mode dominates the powder gas interaction. The intense vaporization dramatically increases the recoil pressure on the powder top surface and a total downward force of ~ 3 N is exerted on the powder (one magnitude larger than the total force in the previous case shown in Fig. 4m). Eventually, the powder dives into the molten pool with a velocity ~ 13 m/s (t = 305 μs). The subsequent disturbance of the molten pool (t = 315 μs – 330 μs) may lead to increased surface roughness and/or mesoscale defects in the build.

In this case, the powder is sequentially subject to the entrainment, elevation/expulsion, and recoil mode. According to our simulation, the occurrence of such a sequence relies on the combination of several events. (i) The powder is heated by the reflected laser beam during its entrainment and reaches a high temperature of ~ 1900 K at t = 245 μs.

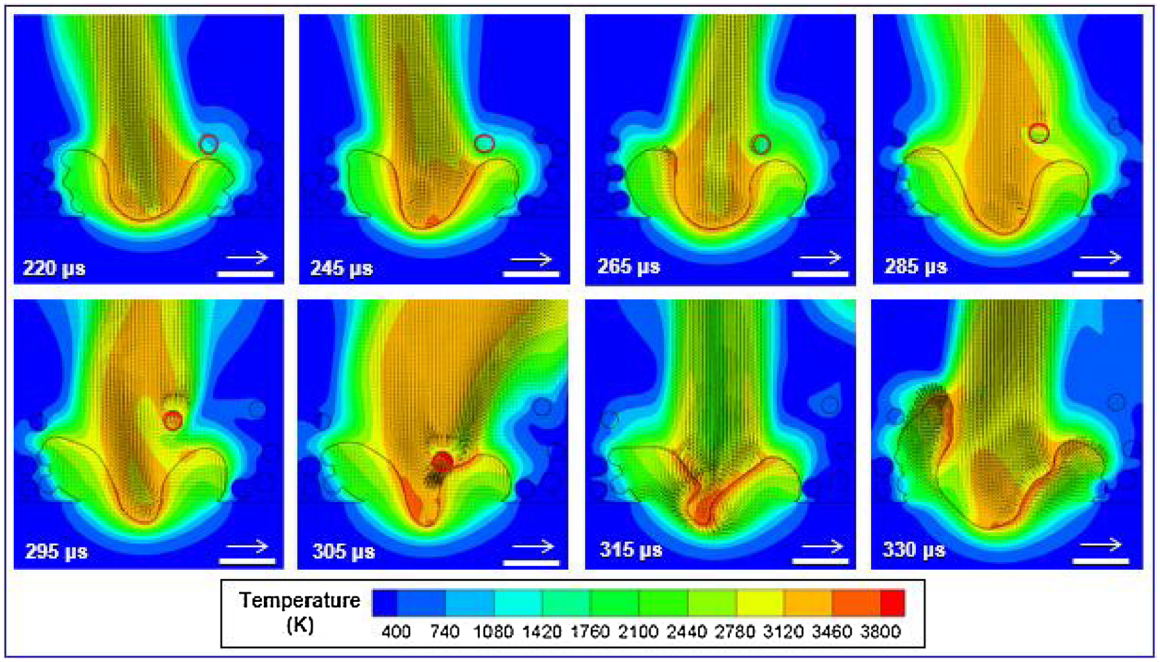

Fig. 6. A time sequence of simulation result demonstrating the recoil mode of powder-gas interaction can interrupt the typical entrainment-ejection motion of powder. Local vaporization occurs on the top surface of the red-circled powder before it can be ejected, leading to the diving motion and significant fluctuation of the molten pool. All the scale bars are 100 μm and arrow keys are 20 m/s for the condensed phase and 2000 m/s for the gaseous phase.

(ii) The powder cuts into the vapor jet with a horizontal velocity ~ 1 m/s at ~ t = 265 μs – 285 μs and is more significantly heated by the direct/reflected laser beam. (iii) Once cutting into the vapor jet, the powder blocks the laser from the molten pool surface underneath. This phenomenon can also be seen in Fig. 4c and 4d. It is argued that such a "shading effect" mitigates the vapor flux from the molten pool surface and delays the ejection of the powder. With these events combined, local vaporization can occur before the powder is ejected away, leading to the diving motion.

3.4. Comparison with high-speed x-ray imaging

High-speed x-ray imaging experiments on LPBF confirm the findings from multi-physics simulations. Four representative powders (*P1 – P4*) are examined from the time sequences shown in Fig. 7a and 7b. The trajectories and velocities of these powders are measured and plotted in Fig. 7c and 7e, respectively. It is noted that these measurements are two-dimensional projections of the three-dimensional powder motions. The trajectories of the four powders circled in red in Fig. 5a, Fig. 6, Fig. 3a, and Fig. 5b are plotted in Fig. 7d, with their velocities recorded in Fig. 7f. For a better comparison, the simulated powder trajectories are sometimes mirrored with respect to the laser center in Fig. 7e.

The experimentally observed powder trajectories substantiate the four powder-gas interaction modes identified from simulations. The trajectory of *P1* resembles the red-circled powder in Fig. 5a, indicating that its behavior is governed by the elevation mode. The downward motion of *P2* (at 300 μs in Fig. 7a) indicates that the metal vaporization occurs at its top surface. Therefore, *P2* is subject to the recoil mode at 300 μs, similar to powder circled in red in Fig. 6. *P3* demonstrates the typical sequence of entrainment-ejection motion, as the powder circled in red in Fig. 3a. Finally, the ejection of *P4* coincides with the existence of a highly unsymmetrical molten pool (as in Fig. 5b), so the tilted vapor jet expels *P4* at a large divergence angle, an expulsion mode governed behavior. It is also observed that, the magnitudes of the simulated particle speed in Fig. 7f reasonably agree with the measured projected velocities of these powders on the imaging plane (Fig. 7e). We note that these velocity magnitudes also reasonably agree with the experimental measurements in [4].

4. Discussion

There are three major forces that drive the powder motion, as summarized in Table 3. The recoil force on the powder surface is induced by the metal vaporization. The pressure drag and friction drag stem from the gas flow around the powder, as the surrounding flow tends to "drag" the powder to move along its direction. The pressure drag is caused by the momentum change of gas when it flows passing the powder, while the friction drag is associated with the boundary layer developed near the powder surface. The magnitudes of pressure drag and friction drag are comparable, which are determined by the speed of the surrounding flow. The speed of the ambient Argon flow is usually one or two orders smaller than the vapor jet. Therefore, the drag forces in the entrainment mode is one or two orders smaller than in the expulsion mode. The recoil force only exists when metal vaporization occurs on the powder surface, and it typically dominates over the drag forces when they coexist. The magnitude of the recoil force depends on the severity of the vaporization; typically, it resembles the drag forces of powder in the elevation mode but can be one or two orders larger when intense vaporization occurs.

Our simulation predicts a maximum vapor jet velocity of ~ 850 m/s (Mach number is ~ 0.7), which agrees with the simulations by others [3,11]. Different from the steady state simulations, the vapor jet flow in our model is fairly unsteady. Its structure is affected by the dynamic evolution of the molten pool and the transient powder motions. For example, the vapor jet can tilt away from the laser incidence due to the unsymmetrical molten pool shape (Fig. 5b), and the width of the jet can be reduced when entrained powder partially blocks the laser (Fig. 3a, 110 μs – 165 μs). The largest Reynolds number of powders is estimated to be ~ 50 (see Appendix A). This disagrees with the estimation given in [5], presumably because the temperature-dependence of gas density and viscosity was not considered in that works. With the relatively "medium" Reynolds number calculated with our model, the motion of powders in LPBF process is likely to follow a laminar flow, rather than a turbulent flow [5] or a Stokes flow [4].

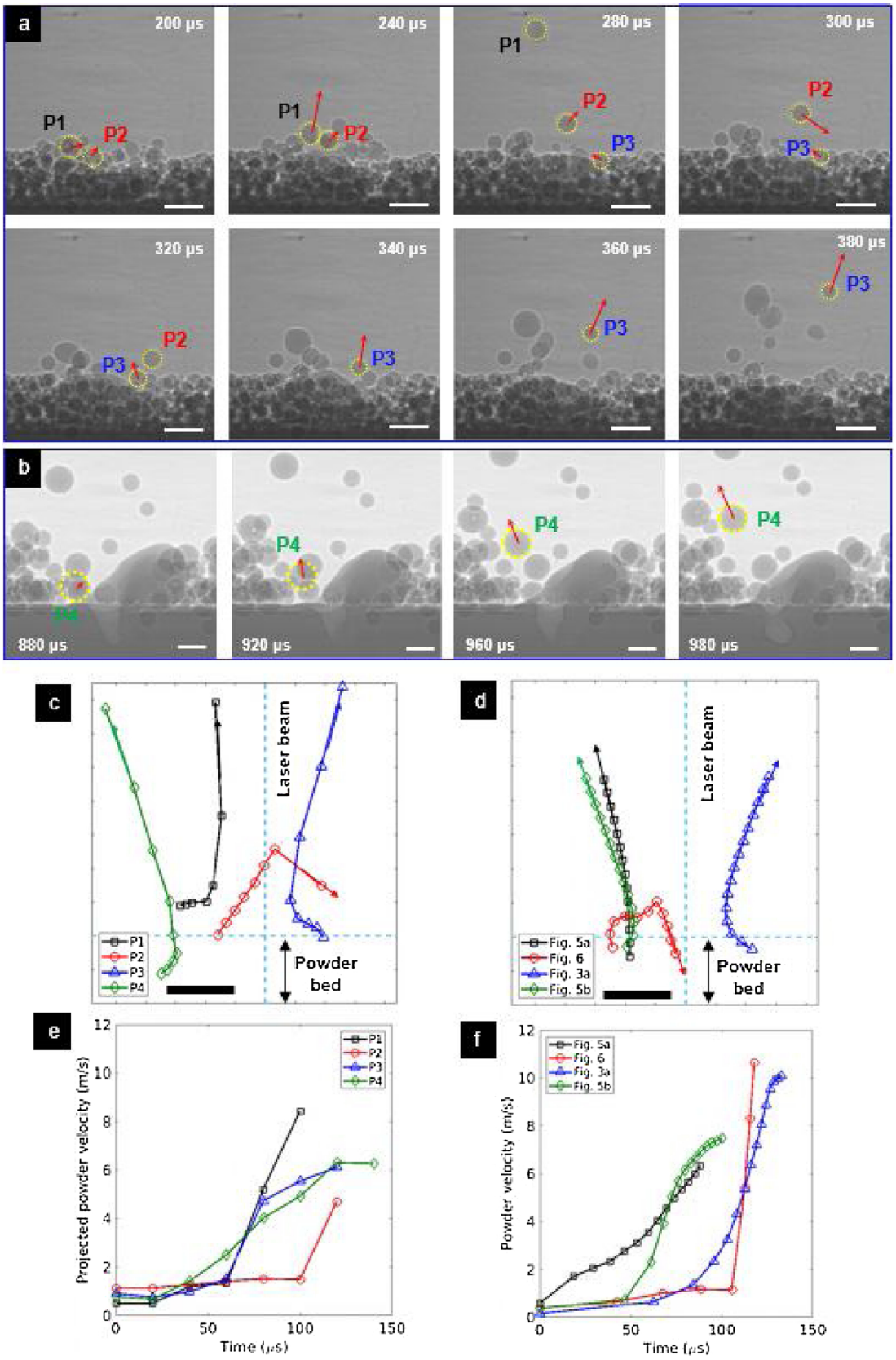

Fig. 7. Comparison between experiments and simulations. (a) and (b) Two time sequences of x-ray imaging with comparable setups as the multi-physics simulations. Four powders (*P1 – P4*) are selected as the representative powders. (a) is adapted from [1]. Powder size is 4-45 μm in (a) and 50-100 μm in (b). (c) Trajectories of *P1 – P4*. (d) Projected powder velocities on the image plane versus time. (e) The trajectories of the four powders circled in red in Fig. 5a, Fig. 6, Fig. 3a, and Fig. 5b for comparison with experiments. Powder trajectories are sometimes mirrored with respect to the laser center. (f) The powder velocities versus time for the simulations. All the scale bars are in 100 μm.

Table 3
Summary of force magnitudes in different modes of powder-gas interaction.

	Recoil Mode	Entrainment Mode	Elevation Mode	Expulsion Mode
Recoil Force (N)	0.1 (5)	0	0	0
Pressure Drag (N)	0.01 (0.1)	0.01	0.1	0.5
Friction Drag (N)	0.01 (0.1)	0.01	0.1	0.5

These force magnitudes are estimated from the 20 simulations conducted. For the recoil mode, the typical magnitudes vary in a wide range; the typical small values are given with the typical large values indicated in brackets.

Significant increase of the powder temperature during its entrainment-ejection process has been reported previously, which suggested a maximum powder temperature above 3000 K [4]. This value agrees with the results in the current work (Fig. 3a and Fig. 6). It was observed in [30] that the entrained powders could melt before they contacted the vapor jet, and the authors suggested that the powder heating can be due to the hot surrounding gas and the reflected laser beam. Here, the current work confirms that the dominating heating mechanism can only be the laser incidence. Using a Reynolds number of 50, the convective heat transfer from the hot surrounding gas to the powder is estimated to be $\sim 10^6$ W/m^2 (see Appendix B), which is much smaller than the power density of laser heating, which is $\sim 10^9$ W/m^2 (Fig. 4a–d). With these heat fluxes, the time needed to fully melt a powder by convective heat transfer only is estimated to be 40,000 μs (Appendix B) which is about two magnitudes larger than the laser pulse duration. The time needed to fully melt a powder by laser incidence only is estimated to be 40 μs. It is therefore argued that the dominating heating mechanism to trigger powder melting is the laser incidence on the powder surface.

For the first time, it is captured in our simulation that the molten pool can be significantly disturbed by the entrance of a high-velocity powder (Fig. 6). In previous work [4], similar “diving” motion of powder was found in the case of a scanning laser, but the effect of such powder motion on the molten pool was not discussed. The fluctuation of the molten pool in LPBF can lead to build inaccuracy, which should thereby be mitigated. If a deep vapor depression (i.e., keyhole) exists, its instability can create porosity and spatters [31–33].

5. Conclusion

In this work, a simulation framework is developed to quantify the powder gas interaction in LPBF. Such quantification is then substantiated by the high-speed synchrotron x-ray imaging experiments. The model uses a computational fluid dynamics module to calculate the thermo-fluid flows in the molten pool and surrounding gases, the level-set method to track the evolution of interface between condensed and gaseous phases, and the Lagrangian particle tracking technique simulate the rigid-body motion of the powders due to the gas flow. The model is able to capture the dynamic evolution of molten pool and depression zone as well as the powder behavior. The simulations results are quantitatively compared with the observations from the high-speed synchrotron x-ray imaging experiments.

The force on the powder surface is primarily induced by the spatial variation of gas pressure around the powder and the viscous force by the surrounding gas flow. According to the direction of the gas-induced forces, four modes of powder-gas interaction are identified.

- The recoil mode is defined when the total force on the powder is pointing downwards, which drives the powder to move downward and merge into the molten pool.
- The entrainment mode is defined when the total force is pointing towards the vapor jet, which drives the powder to move toward the vapor jet.
- The elevation mode is defined when the total force is pointing upwards, which drives the powder to eject with a relatively small divergence angle.
- The expulsion mode is defined when the total force deviates from the upward-pointing direction with a certain angle, which drives the powder to eject with a relatively large divergence angle.

The powder can experience a sequence of interaction modes during its lifespan. In one typical case, the powder is sequentially subject to the entrainment, elevation, and expulsion mode, and accordingly it moves towards the vapor jet and is then ejected at a certain divergence angle. In another typical case, the powder is sequentially subject to the entrainment, elevation (or expulsion), and recoil mode, and accordingly it moves towards the vapor jet and then dives into the molten pool.

The current simulation framework provides a powerful tool to reveal the mechanisms of powder motions in LBPF. Such simulations can potentially provide guidelines for the mitigation of powder motions. Specifically, the simulations can explore a wider range of process parameters to guide experimental parametric studies, such as varying the powder layer thickness [2], laser power and scanning velocity [3], protection gas material [34] and pressure [34,35], and powder material [4].

CRediT authorship contribution statement

Xuxiao Li: Software, Data curation, Formal analysis, Writing - original draft. **Cang Zhao:** Validation, Data curation, Formal analysis. **Tao Sun:** Project administration, Validation, Writing - review & editing. **Wenda Tan:** Conceptualization, Project administration, Writing - review & editing.

Declaration of Competing Interest

The authors declare that they have no known competing financial interests or personal relationships that could have appeared to influence the work reported in this paper.

Acknowledgement

X.L and W.T wish to gratefully acknowledge the financial support provided by the National Science Foundation under Grant No. CMMI-1933368 and the technical support from the Center for High-Performance Computing at the University of Utah. The authors also thank Kamel Fezzaa and Alex Deriy at the Advanced Photon Source for their assistance in the x-ray experiments. This research used resources of the Advanced Photon Source, a U.S. Department of Energy (DOE) Office of Science User Facility operated for the DOE Office of Science by Argonne National Laboratory under Contract No. DE-AC02-06CH11357.

Appendix A. Reynolds number estimation for powders surrounded gas flow in LPBF

Here we defined the powder Reynolds number as in a flow-around-cylinder/sphere problem:

$$Re = \frac{\rho U D}{\mu} \tag{A1}$$

Here ρ is the gas density, U is a characteristic velocity of gas flow, D is the diameter of powder (setting to be 30 μm), and μ is the viscosity of the gas. We note that ρ is a function of and μ are functions of the gas temperature T (Table 2). U can vary significantly depending on the relative position

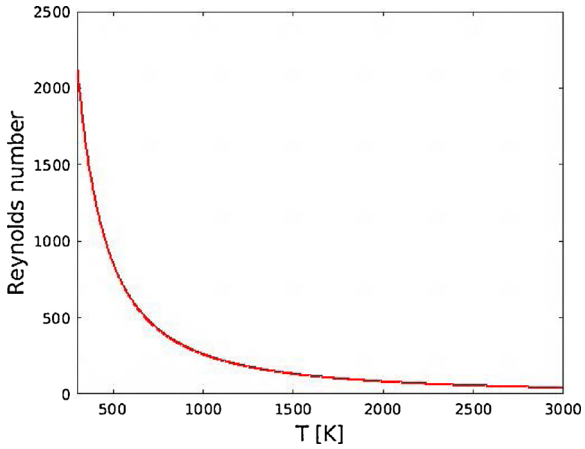

Fig. A1. The powder Reynolds number as a function of temperature. The characteristic gas flow velocity U is 1000 m/s, the powder diameter is 30 μm, and the pressure in the gas is assumed to be 1 atm. The gas density follows ideal gas law, and the gas viscosity follows Sutherland's law (Table 2).

between the powder and the jet flow. Here we want to estimate the maximum possible Reynolds number when the powder is in the vicinity of the vapor jet. From the simulation, we estimate the maximum velocity of the gas flow surrounding the powder to be ~ 1000 m/s. Also, it is found that the gas pressure p does not vary significantly from 1 atm in the region away from the molten pool surface. Setting U to be 500 m/s and p to be 1 atm, we can plot the Reynolds number as a function of T, as shown in Fig. A1.

As can be seen from Fig. A1, the powder Reynolds number is highly dependent on the temperature of the surrounding gas. When the gas is at room temperature (300 K), the Reynolds number is large (~ 2000). This number is similar to the estimation in [5] and indicates turbulent flow around the powder. However, when the temperature is high, e.g., 3000 K, as is the case for the red-circled powder in Fig. 3a, the Reynolds number is only ~ 50, which is a medium value and the powder can be subject to only a laminar flow. Since the vapor jet temperature is usually very high, we argue that the medium Reynolds number is a more reasonable estimation.

Appendix B. Convective heat transfer estimation from gas to powder

Here we estimate the convective heat transfer, q''_{conv}, from the surrounding gas to the powder. We simplify the calculation by assuming a flow-around-cylinder problem, where a cylinder with a diameter D of 30 μm is subject to a uniform gas flow. We use the following empirical correlation [36] to estimate the Nusselt number:

$$Nu = CRe^{m}Pr^{1/3}. \tag{B1}$$

Here Re is the powder/cylinder Reynolds number, Pr is the Prandtl number, and C and m are two constants depending on the Reynolds number. The convective heat transfer coefficient is then given by:

$$h = Nu\frac{k}{D}, \tag{B2}$$

where k is the thermal conductivity of gas. The convective heat transfer (per unit area) is given by:

$$q''_{conv} = h(T_\infty - T_{surf}), \tag{B3}$$

where T_∞ is the temperature of gas at infinity and T_{surf} is the surface temperature of powder.

We set $Re = 50, C = 0.683, m = 0.466$ [36], $k = 0.1$ W m^{-1} K^{-1}. We set an aggressive temperature difference between T_∞ and T_{surf} such that the possible maximum value of q''_{conv} can be estimated. Let T_∞ = 3000 K, and T_{surf} = 300 K; h is calculated to be 1293 W m^{-2} K^{-1}, and q''_{conv} is 3.35 × 10^6 W/m^2. It is noticed that the convective heat transfer under this estimation is three magnitudes less than the heat flux into the powder by laser absorption (Fig. 4a–d). This relatively small value of q''_{conv} is due to the medium Reynolds number ($Re = 50$) which is justified in Appendix A.

Next, we evaluate the significance of the heating by the convective heat transfer (q''_{conv}) and by the laser incidence (q''_{laser}) by comparing the time needed to fully melt a powder with only q''_{conv} and q''_{laser}. The total energy needed to fully melt a powder (assumed to be a cylinder with a diameter D of 30 μm) can be approximated as:

$$E_{melt} = \rho_s\frac{\pi D^2}{4}(c_{ps}(T_S - T_0) + L_m), \tag{B4}$$

where ρ_s is the solid density of metal, c_{ps} is the solid heat capacity of metal, T_S is the solidus temperature, T_0 is the initial temperature taken to be 300 K, and L_m is the latent heat of melting. Taken the values in Table 1 for (ρ_s, c_{ps}, T_S, L_m), E_m is calculated to be 4.19 J. We assume the entire powder surface is subject to the convective heat flux q''_{conv}, and the time needed to fully melt a powder by q''_{conv} only is estimated as $t_{conv} = E_{melt}/(\pi D q''_{conv}) = 13286\,\mu s$. For the laser incidence, we take q''_{laser} to be 10^9 W/m^2 and assume only one-fourth of the powder surface can be subject to direct to reflected laser incidence. Then the time needed to fully melt a powder by q''_{laser} is estimated as $t_{laser} = E_{melt}/(0.25\pi D q''_{laser}) = 178\,\mu s$. We note that t_{conv} is about two magnitudes larger than the laser pulse duration (~ 1000 μs) while t_{laser} is only about one fifth of the pulse duration. Therefore, the only heating mechanism that can cause the fully melting of the powder within the pulse duration is the laser incidence on the powder surface.

Appendix C. Supplementary data

Supplementary material related to this article can be found, in the online version, at doi:https://doi.org/10.1016/j.addma.2020.101362.

References

[1] C. Zhao, K. Fezzaa, R.W. Cunningham, H. Wen, F. De Carlo, L. Chen, A.D. Rollett, T. Sun, Real-time monitoring of laser powder bed fusion process using high-speed X-ray imaging and diffraction, Sci. Rep. 7 (1) (2017) 3602.

[2] Q. Guo, C. Zhao, L.I. Escano, Z. Young, L. Xiong, K. Fezzaa, W. Everhart, B. Brown, T. Sun, L. Chen, Transient dynamics of powder spattering in laser powder bed fusion additive manufacturing process revealed by in-situ high-speed high-energy x-ray imaging, Acta. Mater. 151 (2018) 169–180.

[3] P. Bidare, I. Bitharas, R. Ward, M. Attallah, A. Moore, Fluid and particle dynamics in laser powder bed fusion, Acta. Mater. 142 (2018) 107–120.

[4] S. Ly, A.M. Rubenchik, S.A. Khairallah, G. Guss, M.J. Matthews, Metal vapor micro-jet controls material redistribution in laser powder bed fusion additive manufacturing, Sci. Rep. 7 (1) (2017) 4085.

[5] M.J. Matthews, G. Guss, S.A. Khairallah, A.M. Rubenchik, P.J. Depond, W.E. King, Denudation of metal powder layers in laser powder bed fusion processes, Acta. Mater. 114 (2016) 33–42.

[6] H. Gong, K. Rafi, H. Gu, T. Starr, B. Stucker, Analysis of defect generation in Ti–6Al–4V parts made using powder bed fusion additive manufacturing processes, Addit. Manuf. 1 (2014) 87–98.

[7] A.R. Nassar, M.A. Gundermann, E.W. Reutzel, P. Guerrier, M.H. Krane, M.J. Weldon, Formation processes for large ejecta and interactions with melt pool formation in powder bed fusion additive manufacturing, Sci. Rep. 9 (1) (2019) 5038.

[8] S.A. Khairallah, A.T. Anderson, A. Rubenchik, W.E. King, Laser powder-bed fusion additive manufacturing: Physics of complex melt flow and formation mechanisms of pores, spatter, and denudation zones, Acta Mater. 108 (2016) 36–45.

[9] W. Yan, W. Ge, Y. Qian, S. Lin, B. Zhou, W.K. Liu, F. Lin, G.J. Wagner, Multi-physics modeling of single/multiple-track defect mechanisms in electron beam selective melting, Acta Mater. 134 (2017) 324–333.

[10] C. Panwisawas, C. Qiu, M.J. Anderson, Y. Sovani, R.P. Turner, M.M. Attallah, J.W. Brooks, H.C. Basoalto, Mesoscale modelling of selective laser melting: thermal fluid dynamics and microstructural evolution, Comput. Mater. Sci. 126 (2017) 479–490.

[11] A. Masmoudi, R. Bolot, C. Coddet, Investigation of the laser–powder–atmosphere interaction zone during the selective laser melting process, J. Mater. Process. Technol. 225 (2015) 122–132.

[12] Y.A. Mayi, M. Dal, P. Peyre, M. Bellet, C. Metton, C. Moriconi, R. Fabbro, Laser-induced plume investigated by finite element modelling and scaling of particle entrainment in laser powder bed fusion, J. Phys. D Appl. Phys. 53 (7) (2019) 075306.

[13] W. Tan, N.S. Bailey, Y.C. Shin, Investigation of keyhole plume and molten pool based on a three-dimensional dynamic model with sharp interface formulation, J. Phys. D Appl. Phys. 46 (5) (2013) 055501.

[14] W. Tan, Y.C. Shin, Analysis of multi-phase interaction and its effects on keyhole dynamics with a multi-physics numerical model, J. Phys. D Appl. Phys. 47 (34) (2014) 345501.

[15] N. Kouraytem, X. Li, R. Cunningham, C. Zhao, N. Parab, T. Sun, A.D. Rollett, A.D. Spear, W. Tan, Effect of laser-matter interaction on molten pool flow and keyhole dynamics, Phys. Rev. Appl. 11 (6) (2019) 064054.

[16] D. Li, C.L. Merkle, A unified framework for incompressible and compressible fluid flows, Journal of Hydrodynamics, Ser. B 18 (3) (2006) 113–119.

[17] S. Osher, R. Fedkiw, Level Set Methods and Dynamic Implicit Surfaces, Springer Science & Business Media, 2006.

[18] M. Uhlmann, An immersed boundary method with direct forcing for the simulation of particulate flows, J. Comput. Phys. 209 (2) (2005) 448–476.

[19] R.P. Fedkiw, T. Aslam, B. Merriman, S. Osher, A non-oscillatory Eulerian approach to interfaces in multimaterial flows (the ghost fluid method), J. Comput. Phys. 152 (2) (1999) 457–492.

[20] W. Bennon, F. Incropera, A continuum model for momentum, heat and species transport in binary solid-liquid phase change systems—I. Model formulation, Int. J. Heat Mass Transf. 30 (10) (1987) 2161–2170.

[21] S. Venkateswaran, L. Merkle, Analysis of preconditioning methods for the Euler and Navier-Stokes equations, Lecture series-van Kareman Institute for fluid dynamics 3 (1999) B1–B155.

[22] X. Li, W. Tan, Numerical Investigation of Laser Absorption by Metal Powder Bed in Selective Laser Sintering Processes, Solid Freeform Fabrication (SFF) Symposium, Austin, TX, 2016.

[23] S. Pang, X. Chen, W. Li, X. Shao, S. Gong, Efficient multiple time scale method for modeling compressible vapor plume dynamics inside transient keyhole during fiber laser welding, Opt. Laser Technol. 77 (2016) 203–214.

[24] C.J. Knight, Theoretical modeling of rapid surface vaporization with back pressure, Aiaa J. 17 (5) (1979) 519–523.

[25] P. Meakin, R. Jullien, Restructuring effects in the rain model for random deposition, J. Phys. 48 (10) (1987) 1651–1662.

[26] C. Körner, E. Attar, P. Heinl, Mesoscopic simulation of selective beam melting processes, J. Mater. Process. Technol. 211 (6) (2011) 978–987.

[27] R. Glowinski, T.-W. Pan, T.I. Hesla, D.D. Joseph, J. Periaux, A fictitious domain approach to the direct numerical simulation of incompressible viscous flow past moving rigid bodies: application to particulate flow, J. Comput. Phys. 169 (2) (2001) 363–426.

[28] H.R. Norouzi, R. Zarghami, R. Sotudeh-Gharebagh, N. Mostoufi, Coupled CFD-DEM Modeling: Formulation, Implementation and Application to Multiphase Flows, John Wiley & Sons, 2016.

[29] N.D. Parab, C. Zhao, R. Cunningham, L.I. Escano, K. Fezzaa, W. Everhart, A.D. Rollett, L. Chen, T. Sun, Ultrafast X-ray imaging of laser–metal additive manufacturing processes, J. Synchrotron Radiat. 25 (5) (2018).

[30] U.S. Bertoli, G. Guss, S. Wu, M.J. Matthews, J.M. Schoenung, In-situ characterization of laser-powder interaction and cooling rates through high-speed imaging of powder bed fusion additive manufacturing, Mater. Des. 135 (2017) 385–396.

[31] A. Martin, N. Calta, J. Hammons, S. Khairallah, M. Nielsen, R. Shuttlesworth, N. Sinclair, M. Matthews, J. Jeffries, T. Willey, Ultrafast dynamics of laser-metal interactions in additive manufacturing alloys captured by in situ X-ray imaging, Materials Today Advances 1 (2019) 100002.

[32] R. Cunningham, C. Zhao, N. Parab, C. Kantzos, J. Pauza, K. Fezzaa, T. Sun, A.D. Rollett, Keyhole threshold and morphology in laser melting revealed by ultrahigh-speed x-ray imaging, Science 363 (6429) (2019) 849–852.

[33] C. Zhao, Q. Guo, X. Li, N. Parab, K. Fezzaa, W. Tan, L. Chen, T. Sun, Bulk-explosion-Induced metal spattering during laser processing, Phys. Rev. X 9 (2) (2019) 021052.

[34] P. Bidare, I. Bitharas, R.M. Ward, M.M. Attallah, A.J. Moore, Laser powder bed fusion in high-pressure atmospheres, Int. J. Adv. Manuf. Technol. 99 (1–4) (2018) 543–555.

[35] P. Bidare, I. Bitharas, R.M. Ward, M.M. Attallah, A.J. Moore, Laser powder bed fusion at sub-atmospheric pressures, Int. J. Mach. Tools Manuf. 130 (2018) 65–72.

[36] T.L. Bergman, F.P. Incropera, A.S. Lavine, D.P. DeWitt, Introduction to Heat Transfer, John Wiley & Sons, 2011.